Experimental implementation of higher dimensional time–energy entanglement

D. Richart · Y. Fischer · H. Weinfurter

Abstract Qudit entangled states have proven to offer significant advantages with respect to qubit states regarding the implementation of quantum cryptography or computation schemes. Here we propose and experimentally implement a scalable scheme for preparing and analyzing these states in the time–energy degree of freedom of two-photon pairs. Using the scheme, the entanglement of (2×4)-dimensional states is demonstrated.

1 Introduction

Entanglement is an intrinsic property of quantum mechanics which has enabled the realization of classically impossible tasks, such as the implementation of more efficient computation algorithms, provably secure cryptographic schemes and the teleportation of quantum particles. Compared with qubits, the application of qudits, i.e. states defined in a d-dimensional Hilbert space, offers interesting alternatives. For example, they allow the reduction of elementary gates, and consequently of the number of physical information carriers, necessary to perform quantum computational tasks [1]. Moreover, the number of classical bits transmitted per photon pair can be increased by resorting to high-dimensional super-dense coding schemes [2], and the fault-tolerance

D. Richart (✉) · Y. Fischer · H. Weinfurter
Max-Planck-Institut für Quantenoptik, Hans-Kopfermann-Str. 1,
85748 Garching, Germany
e-mail: Daniel.lrichart@mpq.mpg.de

D. Richart · Y. Fischer · H. Weinfurter
Ludwig-Maximilians-Universität, Schellingstr. 4,
80797 München, Germany

bounds for quantum cryptography schemes can be significantly increased, e.g. to error rates of 35% for four-dimensional encoding [3]. In this context we propose and experimentally implement a scalable scheme for preparing and analyzing high-dimensional states in the time–energy degree of freedom of entangled two-photon pairs.

This paper is structured as follows: a short introduction of the theoretical framework will be given in the following. Section 2 describes in detail the experimental setup, with a special focus on the stabilization scheme used. Finally, experimental results demonstrating entanglement between two ququats ($d = 4$) will be presented in Sect. 3.

Since the first proposal for creating time–energy correlated quantum states by Franson [4], they have been used for long-distance distribution and teleportation of entangled states [5, 6] or for the implementation of Quantum Key Distribution (QKD) schemes [7]. As described schematically in Fig. 1, a source of time–energy entangled photons can be any process that coherently emits pairs of photons. Spontaneous parametric downconversion (SPDC) driven by a source of coherent pump photons is such a process. Within the coherence time of each pump photon a continuous superposition of two-photon states $|\Psi\rangle = \int_{t'} |t\rangle|t\rangle \, dt$ defined for an emission time t is created. For the analysis of the state, each photon of a pair is distributed to the two observers Alice and Bob, which are provided with unbalanced interferometers implementing the very same time delay ΔT and additional phase shifts ϕ_A and ϕ_B.

If ΔT surpasses each SPDC photon's coherence time $t_{c,ph}$, the local phase shifts ϕ_A and ϕ_B will not determine the relative intensities at the outputs of the interferometers. Yet, if both parties agree to analyze coincident detections with 0 time delay, they will project the initial state $|\Psi\rangle$ onto a superposition of the two-photon states $|0\rangle_A|0\rangle_B$ (both photons arrived at the detectors along the short arm) and $|1\rangle_A|1\rangle_B$
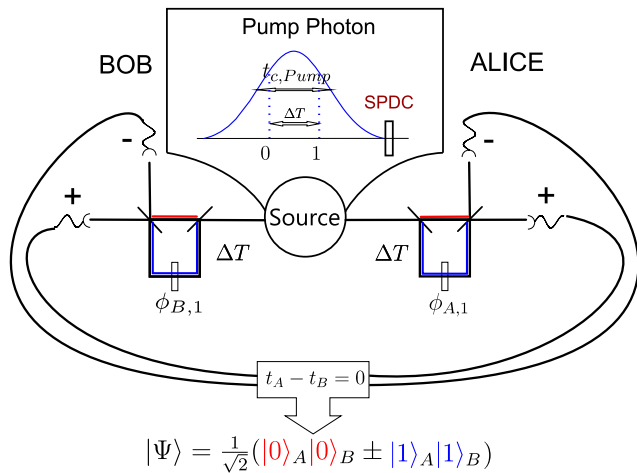
Fig. 1 Scheme for analyzing time–energy entangled two-photon states in two-dimensional Hilbert spaces. A coherent photon pair source is required to produce photon pairs within a continuous range of two-photon emission times. The parties Alice and Bob are each provided with a photon and an interferometer system. A two-dimensional entangled state can be analyzed by performing projection measurements for a time delay $t_A - t_B = 0$ between the detected photons. Each photon can be detected at any of the outputs $\pm$ of the respective interferometer system

(arrival via the long arm):

$$|\Psi\rangle_{2D}^{0\Delta T} = \frac{1}{\sqrt{2}}\big(|0\rangle_A|0\rangle_B + e^{i\cdot(\phi_A+\phi_B)}|1\rangle_A|1\rangle_B\big). \tag{1}$$

They will observe a variation of the coincidence rates in dependence on the relative phases their photons acquire at their respective interferometers according to

$$C_{2D}^{0\Delta T} = \cos^2(\phi_A + \phi_B). \tag{2}$$

This behavior can only be attributed to second-order interference between the two-photon states $|0\rangle_A|0\rangle_B$ and $|1\rangle_A|1\rangle_B$, resulting in the non-classical correlations between the measurement results.

Evidently, such a scheme is not limited to only two possible arrival times. As long as the sum of the delays is sufficiently shorter than the pump coherence time, the effective dimensionality of the state is defined only by the number of delays used in the analyzers [8–10]. Figure 2 depicts how a four-dimensional state can be observed. Here a time–energy correlated state is analyzed by choosing the emission time delays (in multiples of ΔT) $|0\rangle$, $|1\rangle$, $|2\rangle$ and $|3\rangle$ within the coherence time of a pump photon as the four-dimensional computational basis. In analogy to the two-dimensional configuration, spontaneous parametric downconversion can be used to produce two-photon pairs.

They can be analyzed if one photon of a pair is sent to Alice and the other to Bob who are provided with multiple-path interferometer systems designed to project onto the four respective emission times. Here the interferometers are constructed by loops with respective delays ΔT and $2\Delta T$
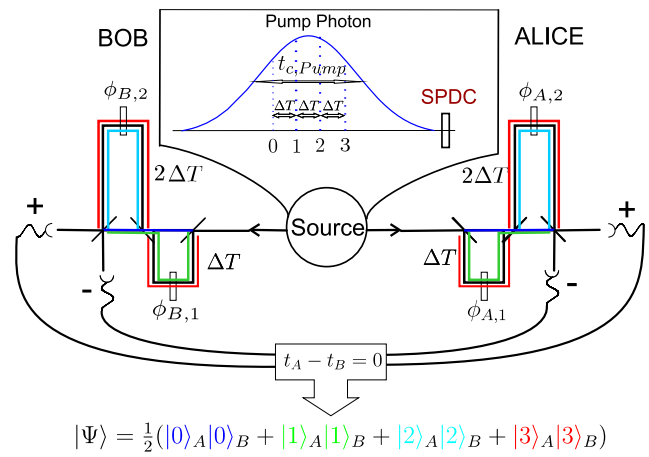

Fig. 2 Scheme for analyzing time–energy entangled two-photon states in higher dimensional Hilbert spaces. Extending the two-dimensional configuration, the parties Alice and Bob use a double-loop interferometer configuration to project onto a superposition of four two-photon detection times $|0\rangle_A|0\rangle_B$, $|1\rangle_A|1\rangle_B$, $|2\rangle_A|2\rangle_B$ and $|3\rangle_A|3\rangle_B$ of a four-dimensional entangled state
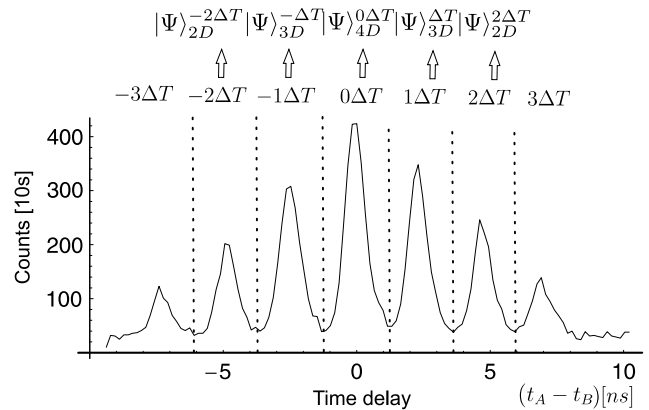

Fig. 3 Time distribution of the coincidence count rates as a function of $t_A - t_B$, Alice's and Bob's photon detection times. For a time delay of 0, coincidence count rates associated to a four-dimensional entangled state can be selected. For delays $\pm\Delta T$ and $\pm 2\Delta T$, a projection onto states with a superposition of three and two two-photon probability amplitudes is realized, displaying correlations of three- and two-dimensional entangled states, respectively. No correlations can be observed in the coincidence windows $\pm 3\Delta T$, corresponding to a projection on a one-dimensional state

such that the probabilities of a photon acquiring a time delay $i\Delta T$, with $i \in [0, 3]$, are equal. They allow us to project onto the two-photon states $|0\rangle_A|0\rangle_B$, $|1\rangle_A|1\rangle_B$, $|2\rangle_A|2\rangle_B$ and $|3\rangle_A|3\rangle_B$, which are indistinguishable for a detection time delay $t_A - t_B = 0$ (see Fig. 3). If the maximal time delay fulfills $3\Delta T \ll t_c$, a coherent superposition can be observed:

$$\begin{aligned}|\Psi\rangle_{4D}^{0\Delta T} = \frac{1}{2}\big(&|0\rangle_A|0\rangle_B + e^{i\cdot(\phi_{A,1}+\phi_{B,1})}|1\rangle_A|1\rangle_B \\ &+ e^{i\cdot(\phi_{A,2}+\phi_{B,2})}|2\rangle_A|2\rangle_B \\ &+ e^{i\cdot(\phi_{A,1}+\phi_{B,1}+\phi_{A,2}+\phi_{B,2})}|3\rangle_A|3\rangle_B\big).\end{aligned} \tag{3}$$

The coincidences between, say, the + output of each interferometer (Fig. 2) show a variation according to

$$C_{4D}^{0\Delta T} = \frac{1}{4} \cos^2\left(\frac{\phi_{A,1} + \phi_{B,1}}{2}\right) \cos^2\left(\frac{\phi_{A,2} + \phi_{B,2}}{2}\right) \quad (4)$$

as a function of their respective relative phase settings $\phi_{A,1}$, $\phi_{A,2}$, $\phi_{B,1}$ and $\phi_{B,2}$ at the ΔT and $2\Delta T$ loops.

Similarly, both parties can agree on measuring coincidence count rates with different time delays, which allows them to project onto two-photon superpositions with a varying number of terms. Here states with the same computational basis as the four-dimensional state but with their respective coincidence functions showing an intrinsic dependence of three- and two-dimensional states are analyzed (see Fig. 3). A projection onto time delays $t_A - t_B = \pm\Delta T$ and $t_A - t_B = \pm 2\Delta T$ allows us to project onto the three- and two-dimensional maximally entangled states

$$|\Psi\rangle_{3D}^{\Delta T} = \frac{1}{\sqrt{3}}\Big(|1\rangle_A|0\rangle_B + e^{i\cdot(\phi_{A,2}+\phi_{B,1}-\phi_{A,1})}|2\rangle_A|1\rangle_B$$
$$+ e^{i\cdot(\phi_{A,2}+\phi_{B,2})}|3\rangle_A|2\rangle_B\Big), \quad (5)$$

$$|\Psi\rangle_{3D}^{-\Delta T} = \frac{1}{\sqrt{3}}\Big(|0\rangle_A|1\rangle_B + e^{i\cdot(\phi_{B,2}+\phi_{A,1}-\phi_{B,1})}|1\rangle_A|2\rangle_B$$
$$+ e^{i\cdot(\phi_{A,2}+\phi_{B,2})}|2\rangle_A|3\rangle_B\Big), \quad (6)$$

$$|\Psi\rangle_{2D}^{2\Delta T} = \frac{1}{\sqrt{2}}\Big(|2\rangle_A|0\rangle_B + e^{i\cdot(\phi_{A,1}+\phi_{B,1})}|3\rangle_A|1\rangle_B\Big), \quad (7)$$

$$|\Psi\rangle_{2D}^{-2\Delta T} = \frac{1}{\sqrt{2}}\Big(|0\rangle_A|2\rangle_B + e^{i\cdot(\phi_{A,1}+\phi_{B,1})}|1\rangle_A|3\rangle_B\Big). \quad (8)$$

For a projection onto the + outputs at the respective interferometers and normalized to the total coincidence count rates, the following rates are obtained for delays $t_A - t_B > 0$:

$$C_{3D}^{\Delta T} = \frac{1}{64}\Big(3 + 2\cos(\phi_{A,1} - \phi_{B,1} - \phi_{A,2})$$
$$- 2\cos(\phi_{A,2} + \phi_{B,2})$$
$$- 2\cos(\phi_{A,1} - \phi_{B,1} + \phi_{B,2})\Big), \quad (9)$$

$$C_{2D}^{2\Delta T} = \frac{1}{16}\Big(1 - \cos(\phi_{A,1} + \phi_{B,1})\Big). \quad (10)$$

In order to expand the dimensionality of the analyzed states, additional interferometer loops are required to double the previous time delays. As an advantage, the construction allows us to increase the number of analyzed emission time delays, and consequently the dimensionality exponentially $\propto 2^N$ (instead of linearly $\propto N$ for similar interferometer proposals [10]), with N the number of interferometer arms. As a drawback, the number of independent phase settings is smaller than the dimensionality of the states. Ultimately, only the pump laser coherence time and the minimal time resolution of the detection system limit the number of

degrees of freedom and consequently the Hilbert space dimension as they impose constraints on the time delays ΔT to be chosen. Alternatively, one can employ time-bin encoding by using a short pump pulse and an interferometric setup for the pump laser equivalent to the analyzer ones [11] or the many mutually coherent pulses of a mode-locked laser [12] (for time-bin-entangled states an additional phase modulator between the source and the interferometers could be added. Here time-dependent phase shifts enable us to apply the phase shifts missing in (3), etc.).

2 Experimental implementation

2.1 General setup

A high-brightness SPDC photon-pair source based on a periodically poled KTP crystal is chosen to produce the entangled photons [13]. A poling period of 9.67 μm and type II degenerate phase matching are used to produce photon pairs with an efficiency of $\eta = 49{,}000\,(\text{s mW})^{-1}$ at a central wavelength of 805.9 nm and with a bandwidth of $\Delta\lambda < 1.1$ nm (corresponding to a coherence time of ≈ 2 ps). The photon pairs are emitted collinearly and the H- and V-polarized photons are separated and coupled into single-mode fibers, respectively.

The implementation of the generic scheme (Fig. 2) was based on various considerations. Fused fiber couplers (FFCs) are used as beam splitters as they warrant a better spatial mode overlap between the different paths (see Fig. 4). This enables a significantly better interference visibility, while requiring only a passive temperature stabilization [5]. As a drawback, the FFCs are less suited for the near-infrared wavelength regime used here than for the Telecom wavelengths for which chromatic dispersion can be compensated routinely. Dispersion is particularly disturbing in this type of interferometer due to the different path lengths in the combined interferometers. Therefore, a hybrid interferometer configuration consisting of a fiber and a free-space path implementing the time delay is chosen, such that both arms of the interferometer share the same path length made of fiber. Polarization-mode dispersion between the different interferometer paths is less severe and is compensated by manual polarization controllers.

The minimal time delay required to distinguish between the different two-photon amplitudes in Fig. 3 depends on the timing resolution of the single photon detection devices. Recently, CMOS-based avalanche detectors (APDs) are reported to reach FWHM timing resolutions down to 50 ps [14]. However, due to the higher detection efficiency in the near infrared, we choose the standard reach-through SPAD (Perkin Elmer, AQ4C-SPCM) with a typical resolution of 500 ps. In order to make the overlap of the two-photon
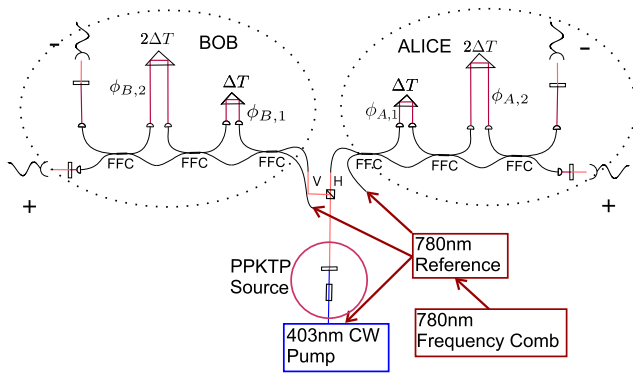
Fig. 4 Experimental setup. Photon pairs are created by pumping a periodically poled KTP crystal using parametric downconversion. The photons are separated at a polarizing beam splitter and sent to the respective interferometer systems both parties (Alice and Bob) require to analyze the shared entangled states. The interferometers are constructed by using fused fiber couplers (FFCs) as beam splitters and a free-space path to implement the required time delays. Finally, single photon avalanche detectors (APDs) are used to detect the photons at each interferometer output

Fig. 5 Interferometer stabilization scheme using polarization multiplexing. An error signal dependent upon the interferometer phase is extracted by ensuring that the polarization transformation for a reference laser is orthogonal in both arms, while the SPDC photons share the same polarization state at the output. It can be used to drive a feedback loop adjusting the relative phase α_{SL} to a constant value while a change $\alpha_{\lambda/2}$ of the analysis $\lambda/2$ waveplate allows us to vary the relative phase acquired by the SPDC photons without any shift of the components inside the interferometer

detection signals negligible, we thus choose $\Delta T > 2.4$ ns. A computer-controlled time-correlation module with a specified resolution of 82 ps (ACAM TDC-GPX) is used for measuring the time differences between the detections at the outputs of each interferometer using four independent APDs. It is believed that further improvements in the detection efficiency and timing resolution of APDs will lead to a significant miniaturization and further scalability of the scheme. Furthermore, the minimal time delay ΔT imposes a strict lower bound for the coherence time of the SPDC pump laser. For that purpose, we use a grating-stabilized blue laser diode at 402.8 nm offering a coherence time of 2.58 μs $\gg \Delta T$.

Alice's and Bob's interferometer delays ΔT and $2\Delta T$ are equalized with respect to each other within the coherence time of their photons to enable the indistinguishability of the respective two-photon probability amplitudes. Similar adjustments are made to equalize the $2\Delta T$ delays to double those of ΔT (Fig. 4).

2.2 Interferometer stabilization

In order to warrant a stable phase relation in the interferometers over longer measurement times, a stabilization scheme compensating thermal and mechanical drifts of each interferometer has been developed.

2.2.1 Polarization-multiplexing scheme

As described before, time–energy correlated states offer an intrinsic insensitivity to the global phase acquired during the transmission of the photons to the respective analysis devices. Nevertheless, the fluctuation of the various phases
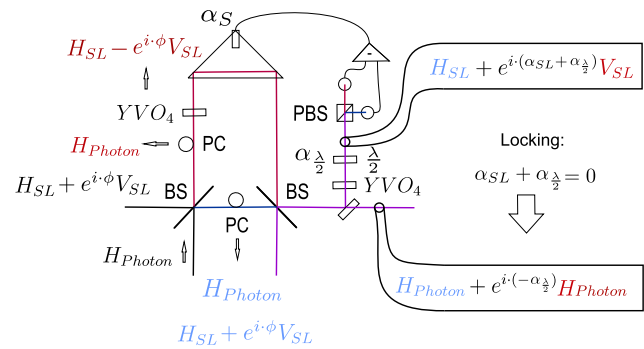
of the unbalanced interferometers during the measurement time will cause a reduction or even loss of interference visibility. The variation $\Delta\phi$ of the relative phases depends on the fluctuation of the path-length difference ΔL and wavelength variation $\Delta\lambda_p$ of the pump laser. As temperature drifts and vibrations of the optical components will cause a variation of both parameters ΔL and $\Delta\lambda_p$, total path-length differences of up to 2 m require a stabilization scheme.

$\Delta\lambda_p$ is minimized by referencing the pump laser diode to a stabilized reference cavity using the Hänsch–Couillaud locking scheme. The cavity itself is stabilized by a grating-stabilized laser diode at 780 nm locked itself to a frequency-comb mode (250 kHz FWHM, 780-nm central wavelength, maser referenced) [15]. The same laser diode is used to stabilize each interferometer to a subwavelength accuracy by using polarization multiplexing (depicted in Fig. 5).

Polarization multiplexing can be used for stabilizing standard interferometers as well as for the system implemented here, for which the reference laser and photon modes spatially overlap [16]. For similar methods, fringe locking on the reference laser interference signal would limit the range over which a stable interferometer phase change is possible, and also requires the measurement of the intensities at both outputs of the respective interferometer. Instead, for polarization multiplexing it suffices to make the polarization states of the stabilization laser in both arms mutually orthogonal, while the polarization state of the SPDC photons should not be changed (in this example H). Thus, manual fiber polarization controllers (PCs) are used first for equalizing the polarizations of the SPDC photons in the respective interferometer paths. The stabilization laser is then coupled into one input of the interferometer polarized with 45°. The rotation of its polarization vector to −45° is induced along the long arm (red) using a birefringent crystal (here YVO$_4$)

with optical axes orientation along H. This leaves the SPDC photon's polarization H unchanged.

In this experiment, wavelengths of 780 nm and 806 nm are chosen for the stabilization laser and SPDC photons, respectively, allowing separation by a dichroic beam splitter. The polarization analysis of the stabilization laser consists of an YVO_4 crystal used to compensate for an additional phase ϕ acquired in the fibers and the dichroic beam splitter and a $\lambda/2$ waveplate before projecting onto a polarizing beam splitter (PBS) which reflects V (vertical) and transmits H (horizontal) polarized light. The polarization change by the waveplate rotation adds to the interferometer phase resulting in the error signal $E(\phi_{SL}, \phi_{\frac{\lambda}{2}}) \propto \cos(\phi_{SL} - 2\phi_{\lambda/2})$ extracted by measuring the difference of the intensities H/V at both outputs of the PBS (ϕ_{SL} is the relative phase difference mod 2π between the interferometer arms, and $\phi_{\lambda/2}$ is the rotation angle of the $\lambda/2$ analysis waveplate). A P–I feedback control is applied to piezoelectrically lock the phase ϕ_{SL} to 0, such that a rotation of $\phi_{\lambda/2}$ will contribute to an effective phase change $-\phi_{\lambda/2}$ acquired by the 806-nm photons. Using this method, we observe fluctuations of the error signal of each interferometer loop with $\Delta\phi_{SD} \leq \pm0.02\pi$, resulting in a relative stability of all four loops of $\Delta\phi_{SD} \leq \pm0.059\pi$ as determined from coincidence measurements over one hour (see Fig. 7).

We want to emphasize that for our method the phase-change speed is ultimately limited by typical millisecond piezoactuator response times, while the probability of fringe skipping is minimized with respect to other stabilization schemes. More importantly, no optical component is placed in the path of the photons in order to vary their phase, therefore avoiding transmission losses and mode aberrations for the SPDC photon modes.

2.2.2 Time-multiplexing scheme for stabilization of different interferometer arms

Figure 6 describes how the polarization-multiplexing scheme can be applied in order to extract error signals dependent on the respective phases ϕ_1 and ϕ_2 caused by the two interferometer loops ΔT and $2\Delta T$.

The H-polarized photons obtained from the SPDC source are coupled into one input, and fiber polarization controllers are placed in each path to obtain H polarization at each output of the fibers. In order to obtain independent error signals SL1 and SL2, the stabilization laser intensity is split up into two modes.

The first component (SL1) used to stabilize ΔT is coupled into the free interferometer input and extracted at the long path of the $2\Delta T$ interferometer using a dichroic beam splitter with ideal transitivity for 806 nm and a 30–70% splitting ratio for 780 nm. The error signal $E(\phi_1, \phi_{1,\frac{\lambda}{2}}) \propto$
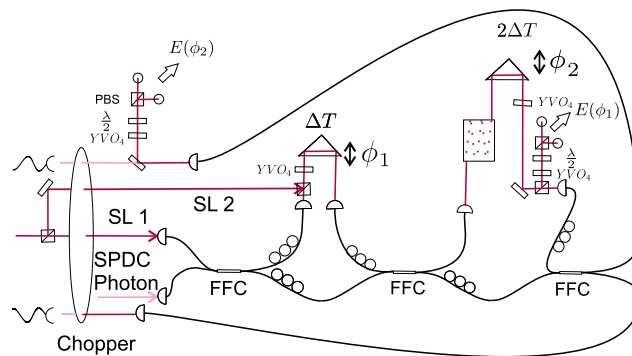

Fig. 6 Time-multiplexing scheme of stabilization laser intensities SL1 and SL2 for stabilizing of different interferometer loops independently. The electronically demultiplexed error signals depend only on the respective phase settings ϕ_1 and ϕ_2 of the delays ΔT and $2\Delta T$, allowing an independent stabilization and variation of the relative phases acquired by the photons. Here the interferometer delay $2\Delta T$ is added by using an optical delay line between two mirrors

$\cos(\phi_1 + \phi_{1,\frac{\lambda}{2}})$ can be extracted by applying the scheme described in Fig. 5. For referencing $2\Delta T$, the intensity SL2 is coupled through the free-space path of the first interferometer using a dichroic beam splitter with the same characteristics. The intensities for SL2 are extracted by interference filters after their overlap at the last beam splitter. The corresponding error signal displays a dependence only on the phase ϕ_2 acquired at the $2\Delta T$ interferometer: $E(\phi_2, \phi_{2,\frac{\lambda}{2}}) \propto \cos(\phi_2 + \phi_{2,\frac{\lambda}{2}})$. The variation of $\phi_{1,\frac{\lambda}{2}}$ and $\phi_{2,\frac{\lambda}{2}}$ allows an independent variation of the relative phases acquired by the SPDC photons in both interferometer arms.

As the stabilization light for the two loops would mutually disturb the generation of the error signals, they are time multiplexed (100-Hz frequency, offset >20 ms) by transmitting each mode through alternating blades of an optical chopper before feeding the laser light into the interferometers. For demultiplexing the respective error signals depending on the phases ϕ_1 and ϕ_2, the P–I feedback electronics are driven by analog sample-and-hold circuits triggering a feedback loop only at the times at which the respective stabilization signals are detected.

Despite the chromatic filtering between the stabilization laser and the SPDC photons, non-negligible background counts are still measured at the wavelength of 806 nm. It is believed that they can be associated with scattering processes of the stabilization laser in the fibers and other optical components. For this reason, the detection of SPDC photons and the transmission of both reference signals SL1 and SL2 are also time multiplexed with respect to each other, by transmitting the SPDC photons through a further set of blades of the same optical chopper. To minimize losses in the photon coincidence count rates, the time-averaged transmission rate of the SPDC photons is set to $\approx75\%$ while the stabilization signals share $\approx25\%$ of the time. The scheme
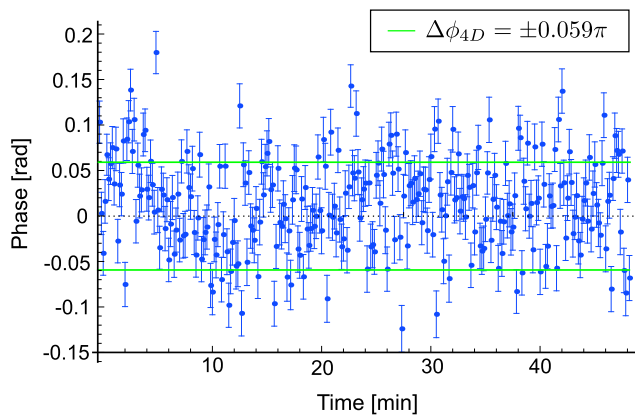
Fig. 7 Phase fluctuation of the four-dimensional coincidence rate over measurement times of up to one hour. Routinely a standard deviation of $\Delta\phi = \pm 0.059\pi$ is observed

is scalable and can be applied on additional interferometer arms used to expand the dimensionality of the analyzed states.

3 Experimental results

First, we evaluate the performance of the stabilization scheme by analyzing the time-dependent variation of the coincidence count rates for the four-dimensional state. Typical phase deviations for measurement times of up to 50 min and integration times of 10 s are displayed in Fig. 7. Average standard deviations of $\Delta\phi_{4D} = \pm 0.059\pi$ are observed, ≈ 3 times larger than for the single-interferometer stabilization scheme of $\Delta\phi_{PM} = \pm 0.02\pi$ described in Sect. 2.2.1, but still sufficiently small for further measurements. The main contribution to this value is due to the independent fluctuations of four interferometer phases (see (3)) and the additional phase uncertainty resulting from the short time span used for stabilization ($\approx 8\%$).

In order to characterize and to evaluate the setup, first the dependence of the coincidence count rates of (4), (9) and (10) for different dimensions is tested for phases ϕ_1 and ϕ_2 for each party. An illustrative way to display the difference between two-dimensional and four-dimensional entangled states is to simultaneously scan the phases $\phi_{A,1}$ and $\phi_{A,2}$ of Alice's interferometers ($\phi_{B,1} = \phi_{B,2} = 0$). Then the coincidence functions as given in (3) and (9) simplify to $C_{4D}^{0\Delta T} \propto \cos\phi^4$ and $C_{2D}^{2\Delta T} \propto \cos\phi^2$, respectively. As illustrated in Fig. 8, the coincidence count rates clearly show an excellent overlap with the function $C_{4D}^{0\Delta T}$. As described in [17, 18] these characteristics can be used to define dimensional witnesses.

Next, we analyze the coincidence count rates observed for states of different dimensions by comparing the experimental data with the corresponding theoretical predictions.
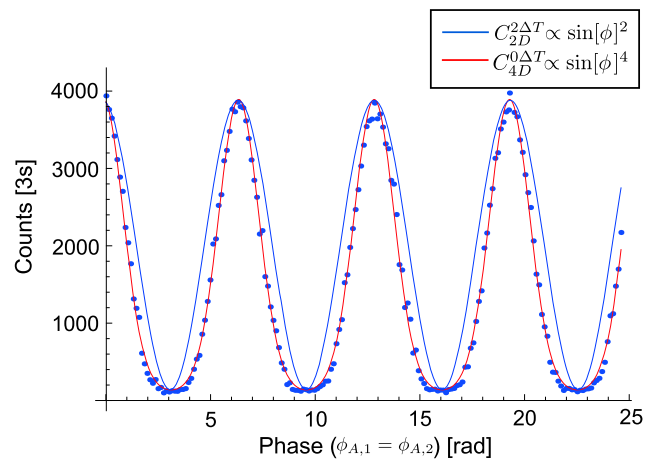

Fig. 8 Coincidence count rate variation for a simultaneous scan of phases $\phi_{A,1}$ and $\phi_{A,2}$ in both interferometer arms of Alice. The function $C_{4D}^{0\Delta T}$ is fitted to the experimental data while $C_{2D}^{2\Delta T}$ corresponds to the theoretical coincidence function for a two-dimensional state

In Fig. 9 the coincidences for the $+, +$ detector combination are shown as a function of $\phi_{A,2}$ for Figs. 9(a) and 9(b) and in dependence on $\phi_{A,1}$ for (c) and (d) while keeping the respective other phases constant at 0. In (a) and (b), the fringe visibility for the four-dimensional data (blue) amounts to $V_{4D} = 0.981(8)\%$ while the corresponding value for the three-dimensional state (green) only amounts to $V_{3D} = 0.654(7)\%$ and vanishes for the two-dimensional state (red), in close correspondence with the theoretical predictions of $V_{4D,th} = 1$, $V_{3D,th} = 7/9 = 0.78$ and $V_{2D,th} = 0$ according to (3), (8) and (9). The phase difference between both coincidence count rates of $\Delta\phi = \phi_{3D} - \phi_{4D} = 1.024(2)\pi$ corresponds closely to the theoretical expected value of π. In contrast, when varying $\phi_{A,1}$ (Figs. 9c and 9d), the three-dimensional coincidence function remains constant at $1/9$ of the maximal probability, while the two-dimensional coincidence count rate displays a visibility of $V_{2D} = 0.919(11)\%$, in clear correspondence with the theoretical expectations ($V_{2D,th} = 1$). Again, the phase difference $\Delta\phi = \phi_{2D} - \phi_{4D} = 1.013(2)\pi$ displays the good reproducibility of the interferometer setup. The periods of all curves show a deviation of less than $\approx 4\%$ with respect to the ideal value. A contribution of accidental coincidence count rates in the range of 1% of the maximal count rates of the four-dimensional state is observed, resulting in a negligible reduction of its interference visibility. For the two-dimensional state, the count rates are reduced by a factor of four as compared to the four-dimensional state (see (9)); the same background causes a significantly lower signal/noise ratio and a higher reduction of the visibility.

A figure of merit for the suitability of the setup for preparing higher dimensional time–energy entanglement is

Fig. 9 Experimental and theoretical coincidence probabilities for four-dimensional, three-dimensional and two-dimensional states as a function of $\phi_{A,2}$ (**a** and **b**) and $\phi_{A,1}$ (**c** and **d**)
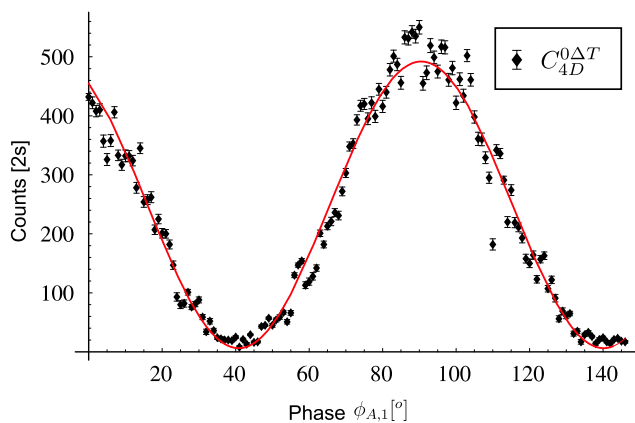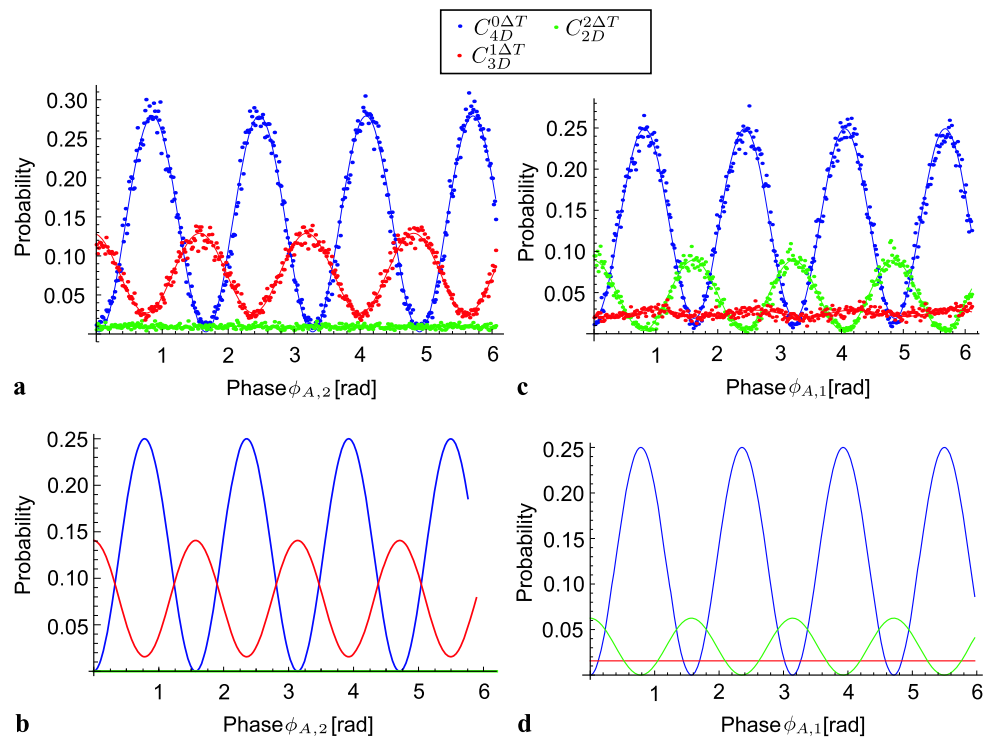

Fig. 10 Coincidence count rate of the four-dimensional entangled state scanned as a function of the phase $\phi_{A,1}$ of Alice's short interferometer

the interference visibility of the coincidence curves. Following the considerations given in [19], a Bell inequality can be defined [18], which is violated only by (2×4)-dimensional entangled states. Here the bound $I \leq 2$ can be translated into a minimal fringe visibility of $V_c = 78.4\%$ to allow a violation of local realism for the state space spanned by our interferometer system. The experimentally determined visibility (Fig. 10) of $V_{\exp} = 0.975(16)\%$ surpasses the bound by 12 standard deviations, offering the potential for a violation of higher dimensional Bell inequalities [18].

4 Conclusion

We introduced an experimental scheme which is suited for the preparation and analysis of four-dimensional entangled photons. The experimental results exhibit high visibilities and are in good agreement with the described theoretical predictions, enabling the expansion of the scheme to entangled states of even higher dimensions. From the viewpoint of fundamental research, they offer the opportunity for studying the increased non-classicality of high-dimensional states as characterized by the violation of Bell tests [18, 20] or allow studies of the non-contextual nature of quantum mechanics [21–23]. With increasing dimensionality of the encoded states, the application of mutually unbiased bases allows us to increase the security bounds of quantum cryptography schemes [20] while minimizing the experimental effort for full state determination [24] with respect to standard tomographic techniques. It is thus of high relevance to utilize the benefits of the scheme demonstrated here and to further increase the dimensionality of qudit states.

References

1. B.P. Lanyon, M. Barbieri, M.P. Almeida, T. Jennewein, T.C. Ralph, K.J. Resch, G.J. Pryde, J.L. O'Brien, A. Gilchrist, A.G. White, Nat. Phys. **5**, 134 (2009)

2. J.T. Barreiro, T.-C. Wei, P.G. Kwiat, Nat. Phys. **4**, 282 (2008)
3. G.M. Nikolopoulos, K.S. Ranade, G. Alber, Phys. Rev. A **73**, 032325 (2006)
4. J.D. Franson, Phys. Rev. Lett. **62**, 2205 (1989)
5. W. Tittel, J. Brendel, B. Gisin, T. Herzog, H. Zbinden, N. Gisin, Phys. Rev. A **57**, 3229 (1998)
6. I. Marcikic, H. de Riedmatten, W. Tittel, H. Zbinden, N. Gisin, Nature **421**, 509 (2003)
7. G. Ribordy, J. Brendel, J.-D. Gautier, N. Gisin, H. Zbinden, Phys. Rev. A **63**, 012309 (2000)
8. R.T. Thew, A. Acin, H. Zbinden, N. Gisin, Phys. Rev. Lett. **93**, 010503 (2004)
9. G. Weihs, M. Reck, H. Weinfurter, A. Zeilinger, Phys. Rev. A **54**, 893 (1996)
10. M. Zukowski, A. Zeilinger, M.A. Horne, Phys. Rev. A **55**, 2564 (1997)
11. I. Marcikic, H. de Riedmatten, W. Tittel, V. Scarani, H. Zbinden, N. Gisin, Phys. Rev. A **66**, 062308 (2002)
12. H. de Riedmatten, I. Marcikic, V. Scarani, W. Tittel, H. Zbinden, N. Gisin, Phys. Rev. A **69**, 050304 (2004)
13. A. Fedrizzi, T. Herbst, A. Poppe, T. Jennewein, A. Zeilinger, Opt. Express **15**, 15377 (2007)
14. F. Stellari, IEEE Trans. Electron Devices **48**, 12 (2001)
15. T.W. Hänsch, Rev. Mod. Phys. **78**, 1297 (2006)
16. O. Schulz, R. Steinhübl, M. Weber, B.-G. Englert, C. Kurtsiefer, H. Weinfurter, Phys. Rev. Lett. **90**, 177901 (2003)
17. B.-J. Pors, F. Miatto, G.W. 't Hooft, E.R. Eliel, J.P. Woerdman, J. Opt. **13**, 064008 (2011)
18. D. Richart, Y. Fischer, W. Laskowski, H. Weinfurter, to be published
19. D. Collins, N. Gisin, N. Linden, S. Massar, Phys. Rev. Lett. **88**, 040404 (2002)
20. N.J. Cerf, M. Bourennane, A. Karlsson, N. Gisin, Phys. Rev. Lett. **88**, 127902 (2002)
21. G. Kirchmair, F. Zähringer, R. Gerritsma, M. Kleinmann, O. Gühne, A. Cabello, R. Blatt, C. Roos, Nature **460**, 494 (2009)
22. E. Amselem, M. Rådmark, M. Bourennane, A. Cabello, Phys. Rev. Lett. **103**, 160405 (2009)
23. R. Lapkiewicz, P. Li, C. Schaeff, N.K. Langford, S. Ramelow, M. Wiesniak, A. Zeilinger, Nature **474**, 490 (2011)
24. R.B.A. Adamson, A.M. Steinberg, Phys. Rev. Lett. **105**, 030406 (2010)